

# Theory of charge- $6e$ condensed phase in Kagome lattice superconductors

Tong-Yu Lin<sup>1</sup> and Guang-Ming Zhang<sup>1,2,3,\*</sup>

<sup>1</sup>State Key Laboratory of Low Dimensional Quantum Physics and  
Department of Physics, Tsinghua University, Beijing 100084, China

<sup>2</sup>Collaborative Innovation Center of Quantum Matter, Beijing 100084, China

<sup>3</sup>Frontier Science Center for Quantum Information, Beijing 100084, China

(Dated: June 18, 2024)

Recently the experimental evidence of a charge- $6e$  condensed phase in the kagome superconductor  $\text{AV}_3\text{Sb}_5$  (J. Ge, et. al., Phys. Rev. X 14, 021025 (2024)) has sparked significant interest. At a phenomenological level, the order parameter of the  $3Q$  pair-density-wave state can form either a triangular lattice or a kagome lattice, in which the vortices and antivortices locate at the center of the plaquettes. When the phase of a Cooper pair is denoted as a XY spin, the effective model for the phase fluctuation is characterized by the frustrated XY spin model on a triangular lattice with the nearest neighbour antiferromagnetic coupling or a kagome lattice with both nearest neighbour and next-nearest neighbor antiferromagnetic couplings. While both models produce  $\frac{1}{3}$  fractional vortex excitations, which arise as the kinks on the domain walls in the low-energy excitations, the triangular lattice model has a much larger domain wall energy than the vortex interaction energy, so the frustrated kagome lattice model becomes unique. By developing a state-of-the-art numerical tensor network method, we rigorously solve this effective model at finite temperatures and confirm the presence of a vestigial phase with  $\frac{1}{3}$  vortex-antivortex paired phase in the absence of phase coherence of Cooper pairs, which is dual to the charge- $6e$  condensed phase. Our theory provides a potential explanation for the vestigial charge- $6e$  magneto-resistant oscillations observed in the recent experimental work.

**Introduction.** -The quasi-2D vanadium-based kagome materials  $\text{AV}_3\text{Sb}_5$  (A=K, Rb, Cs) have emerged as a focus of research interest due to their rich phase diagram [1, 2], including charge density wave (CDW) order [3–10] and superconductivity [11–13]. The materials undergo the CDW transition around  $T_{\text{cdw}} \sim 80 - 110$  K. It was proposed that the normal state might have loop current order with the time-reversal symmetry breaking (TRSB) [14, 15], and the superconducting state exhibits exotic features as well. Below  $T_{\text{sc}} \sim 1 - 3$  K, scanning tunneling microscopy (STM) experiment had observed a  $3Q$  pair-density-wave (PDW) order with a  $\frac{4a_0}{3} \times \frac{4a_0}{3}$  spatial modulation superimposed on the background of the  $2a_0 \times 2a_0$  and  $4a_0$  unidirectional CDW ordering [11]. Moreover, the recent magneto-transport experiment [12] in the superconducting fluctuation regime has revealed a potentially more complex superconducting phase diagram. As the temperature gradually increases from the zero resistance, the conventional magnetoresistance oscillation with a period of  $\frac{h}{2e}$  is suppressed, but the periods of  $\frac{h}{6e}$  of magnetoresistance oscillations emerge, indicating the presence of a charge- $6e$  paired ordering phase in the absence of phase coherence of Cooper pairs [12]. These experimental observations pose challenges for theoretical understanding of superconductivity in kagome materials  $\text{AV}_3\text{Sb}_5$ .

It is known that the superconducting state is generally described by the spatial dependent order parameter  $\Delta(r) = |\phi(r)|e^{i\theta(r)}$ . In two dimensions (2D), the superconducting transition is determined by the thermal fluctuation of the Cooper pair phase field [16–19]. For uniform superconducting state, when the amplitude fluctuation is frozen, the phase fluctuation can be simply

described by the classical XY spin model and the phase coherence is characterized by the Berezinskii-Kosterlitz-Thouless (BKT) transition [20–22] with the quasi-long-range order (QLRO) of the field  $e^{i\theta(r)}$ .

From the Ginzburg Landau (GL) free energy, the possible PDW ground state, which displays the hexagonal lattice symmetry and global  $U(1)$  symmetry, has been solved in [23]. To be consistent with TRSB in the normal state, the PDW ground state must be commensurate with the  $2a_0 \times 2a_0$  CDW order, maintaining  $C_6$  rotation symmetry [24, 25]. The general order parameter form of the  $3Q$  PDW state is expressed as

$$\Delta_{\text{pdw}}(r) = \sum_{\pm Q_j} \Delta_{Q_j} e^{iQ_j \cdot r}, \quad (1)$$

where  $\pm Q_j$  denotes the six wave vectors of the PDW state and  $Q_j = \frac{3}{4}G_j$  as the Bragg vectors of the underlying kagome lattice with the lattice constant  $a_0$ . There are two possible PDW states that satisfy these conditions, and their maximum amplitude positions form a triangular lattice and a kagome lattice, respectively.

$$\begin{aligned} \psi_{\text{v-av}}^{\pm}(r) &= \Delta e^{i\theta} \sum_{j=1,2,3} e^{\pm iQ_j \cdot (r-r_0)} \\ \psi_{\text{kagome}}^{\pm}(r) &= \Delta e^{i\theta} \sum_{j=1,2,3} e^{\pm i(j-1)\frac{2\pi}{3}} \cos[Q_j \cdot (r-r_0)], \end{aligned} \quad (2)$$

where  $\Delta e^{i\theta}$  denotes the overall amplitude and phase of the PDW state,  $r_0$  determines the overall position of the PDW state located at the  $C_6$  rotation center of the CDW states. When  $r_0$  is fixed, both ground states exhibit a

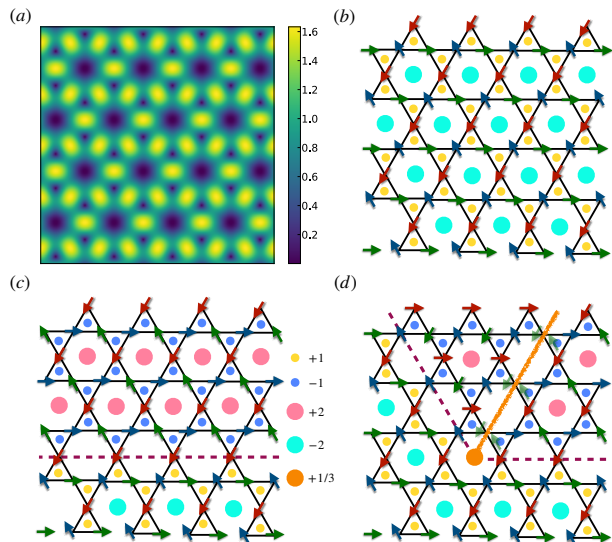


FIG. 1: (a) The amplitude distribution of  $\psi_{\text{kagome}}$ . (b) The phase distribution on the kagome lattice. The pink (cyan) circle denotes  $\pm 2$  vortex. (c) Spin configuration with infinite straight domain wall, depicted by the purple dashed line. (d) The  $+\frac{1}{3}$  vortex excitation at the kink of the domain wall.

$U(1) \times Z_2$  ground state degeneracy, where the  $Z_2$  degeneracy is due to the TRSB. While the  $\psi_{\text{v-av}}^{\pm}(r)$  possess only three non-zero pairing components, when coupled to a uniform superconducting order parameter  $\Delta_0$  [25], these states can also yield the six  $\pm Q_j$  peaks observed in STM experiments [11].

In Fig. 1(a), the amplitude distribution of the superconducting order parameters  $\psi_{\text{kagome}}^+(r)$  is plotted. The positions of the maximum amplitude  $\psi_{\text{kagome}}^+(r)$  form a kagome lattice, while their zeros of amplitude are located at the center of the triangle and hexagonal plaquettes, where  $+1$  vortices and  $-2$  antivortices at the center of triangular and hexagonal plaquettes, respectively. The key feature of this state is captured by the phase distribution on the emergent lattice. As shown in Fig. 1(b), three spins  $(\theta_A, \theta_B, \theta_C)$  on each triangle have a relative phase difference:

$$\theta_B = \theta_A \pm \frac{2\pi}{3}, \theta_C = \theta_A \pm \frac{4\pi}{3}. \quad (3)$$

The vortex distribution in the PDW states can also be described by the vorticity [26], which is a lattice discrete version of the vortex. The vorticity is defined at the plaquette of the lattice:  $v_p = \frac{1}{2\pi} \sum_{i,j \in p} \phi_{ij}$ ,  $\phi_{ij} = (\theta_i - \theta_j) \pmod{2\pi}$ , where the summation is taken in the clockwise direction over the bonds around the plaquette  $p$ . It can be easily verified that the vorticity in the lattice model is consistent with the PDW states.

**Effective model and fractional vortex excitations.** -To describe the phase fluctuation in the presence of vortex-antivortex ground state for  $\psi_{\text{v-av}}^{\pm}(r)$ , the

effective antiferromagnetic (AF) XY spin model on a triangular lattice [27–32] may be considered, and the details include in Supplementary III.B.

For  $\psi_{\text{kagome}}^{\pm}(r)$ , due to the weak geometric constraints on the arrangement of vorticity between the neighboring triangles on the kagome lattice, we have to consider an effective Hamiltonian with both the nearest neighbor and weak next-nearest-neighbor AF interactions on a kagome lattice [33–35].

$$H = J_1 \sum_{\langle i,j \rangle} \cos(\theta_i - \theta_j) + J_2 \sum_{\langle\langle i,j \rangle\rangle} \cos(\theta_i - \theta_j), \quad (4)$$

which favors the ferromagnetic arrangement of vorticity on neighboring triangular plaquettes.

In accordance with the ground state degeneracy, there are two kinds of topological excitations: vortices and domain walls. In Fig. 1(d), we illustrate the spin configurations in the presence of an infinite straight domain wall excitation. When the ground state configuration on one side of the wall is fixed, the vorticity and orientation of spins on the other side of the wall are given by

$$(\theta'_A, \theta'_B, \theta'_C) = (\theta_A, \theta_B + \frac{2\pi}{3}, \theta_C - \frac{2\pi}{3}). \quad (5)$$

Additionally, there exists a third type of topological defect,  $1/3$  fractional vortex excitation as the kink on a domain wall [34]. If the domain wall is not straight but has a  $120^\circ$  kink at the center of one of the hexagonal plaquettes, as shown in Fig. 1(c), the phase configuration on the other side of the wall, after buckling, is given by

$$(\theta'_A, \theta'_B, \theta'_C) = (\theta_A + \frac{2\pi}{3}, \theta_B - \frac{2\pi}{3}, \theta_C), \quad (6)$$

which lead to a global  $\frac{2\pi}{3}$  phase mismatch, characterized by a semi-infinite branch cut passing through the center of the hexagonal plaquette. To compensate for the phase mismatch, all the spins around the kink will rotate by an angle  $\theta \in (0, \frac{2\pi}{3})$ , effectively forming a  $\frac{1}{3}$  fractional vortex.

In fact, the AF triangular lattice XY spin model also exhibits  $\frac{1}{3}$  vortex excitations [29], which can be constructed in the same manner (see Supplementary-Fig.6). However, the fractional vortex is a composite topological excitation that cannot exist without the presence of an infinite domain wall. The excitation energy of these composite objects can be expressed as  $E_{\text{fv}} = E_{\text{dw}}L + \frac{1}{9}E_{\text{v}} \ln L$ , where  $L$  is the system size,  $E_{\text{dw}}$  is the energy per length of the domain wall, and  $E_{\text{v}}$  is the pre-logarithmic factor of the vortex energy, proportional to the superfluid density. For the AF triangular lattice model,  $E_{\text{dw}}$  is of the same order as vortex energy, and the fractional vortices are always bounded by the linear energy cost of the domain wall even when further neighboring interaction is considered [30]. As the temperature increases, the system first undergoes a BKT transition

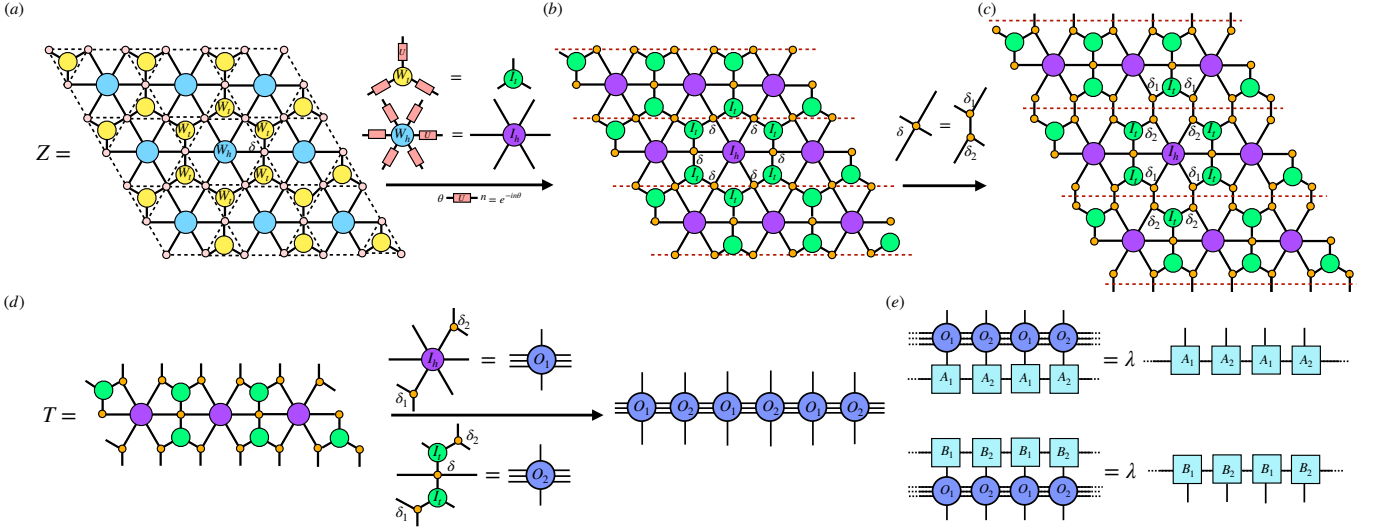


FIG. 2: TN representation of the  $J_1 - J_2$  AF XY spin model. The relationship between local tensors is depicted on the arrows connecting different tensor network diagrams. (a) TN with continuous indices. The dashed lines represent the bonds of the original kagome lattice, while solid lines depict the legs of tensors. (b) TN with discrete indices constructed by Fourier transformation on each plaquette and integration of spin variables. (c) The vertical splitting of the  $\delta$  tensor, with the split bonds shown by red dashed lines. (d) Construction of the transfer matrix and uniform local tensors. (e) Up and down eigenequations for the fixed-point uniform matrix product state (MPS)  $|\psi(A)\rangle$  and  $\langle\psi(B)|$  of the transfer matrix  $T$ .

driven by the unbinding of integer vortex pairs, followed by an Ising transition driven by the proliferation of domain walls [28, 31, 32]. Nevertheless, in the AF kagome lattice model, the energy of a domain wall per length is determined by  $J_2$ . When  $J_1 \gg J_2$ , the proliferation of domain walls occurs first, and the fractional vortex becomes relevant, leading to an intermediate fractional vortex paired phase [34, 36, 37].

**Tensor network method.** -In the TN formalism, the first step is to express the partition function in terms of an infinite tensor network. Since the  $J_1 - J_2$  XY kagome lattice model is a frustrated system, constructing its TN representation requires careful consideration. In our previous work [36], we have established a comprehensive framework for addressing frustrated models with continuous degrees of freedom. This framework can be seamlessly applied to the present case, providing a natural and effective approach.

To account for the vorticity degree of freedom, the global Boltzmann weight  $\exp(-\beta H(\theta))$  can be decomposed into the product of local Boltzmann weights

$$Z = \prod_i \int \frac{d\theta_i}{2\pi} \prod_{t_1} W_{t_1}(\theta_{t_1}) \prod_h W_h(\theta_h), \quad (7)$$

where  $W_t$  and  $W_h$  include the Boltzmann weight of all the nearest-neighbor interactions within an elementary triangle plaquette and a hexagonal plaquette, respectively. The partition function can be translated into a tensor network with continuous  $U(1)$  indices, as shown

in Fig.2(a). To transform the local tensors onto a discrete basis, the Fourier transformations are made on the Boltzmann weights  $W_t$  and  $W_h$ , respectively

$$\begin{aligned} I_{t_1}(n_1, n_2, n_3) &= \prod_{i=1}^3 \int \frac{d\theta_i}{2\pi} W_{t_1}(\theta_1, \theta_2, \theta_3) \prod_{i=1}^3 U(\theta_i, n_i), \\ I_h(n_1, n_2, n_3, n_4, n_5, n_6) &= \prod_{i=1}^6 \int \frac{d\theta_i}{2\pi} W_h(\theta_1, \theta_2, \theta_3, \theta_4, \theta_5, \theta_6) \prod_{i=1}^6 U(\theta_i, n_i), \end{aligned}$$

where  $U(\theta, n) = e^{-in\theta}$  is the basis of the Fourier transformation. Then the original phase variables  $\{\theta\}$  can be integrated out on each site and the partition function is transformed into the TN representation shown in Fig. 2(b).

In Fig. 2(c), we further decompose the  $\delta$  tensor vertically in order to construct the linear transfer matrix

$$\delta_{n_1+n_2+n_3+n_4,0} = \sum_{n_0} \delta_{n_1+n_2-n_0,0}^1 \delta_{n_3+n_4+n_0,0}^2. \quad (8)$$

So the transfer matrix  $T$  can be built by grouping the  $\delta^1, \delta^2, \delta, I_h, I_t$  tensors and contracting them. After that, the transfer matrix is further split horizontally to obtain the local uniform tensors  $O_1$  and  $O_2$ , whose interior structures are shown in Fig. 2(d). Finally the linear transfer matrix is represented as

$$T(k_1, k_2) = \text{tTr}(\dots O_1 O_2 O_1 O_2 \dots), \quad (9)$$

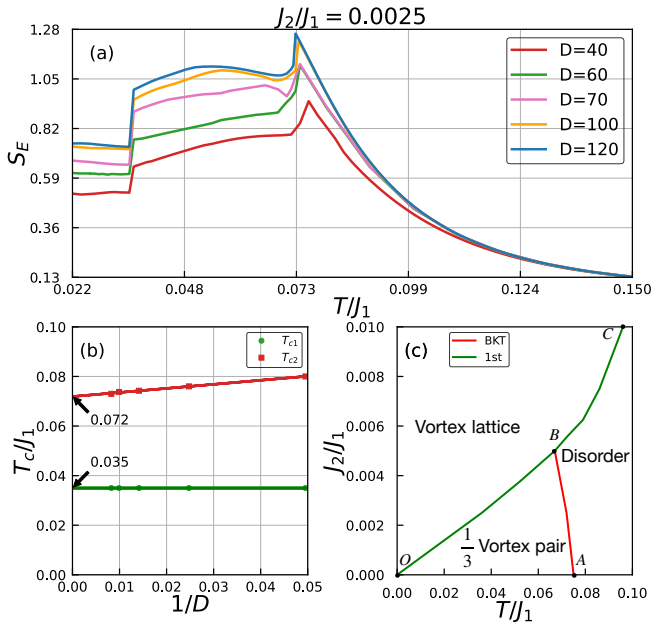


FIG. 3: (a) The generalized entanglement entropy as a function of temperature for  $J_2 = 0.0025J_1$ . (b) The singularity temperatures  $T_{c1}$  and  $T_{c2}$  of the entanglement entropy fitted for MPS bond dimensions from 40 to 120. (c) The phase diagram of the  $J_1 - J_2$  AF XY spin model on a Kagome lattice. The BKT transition line starts from point A (0.075, 0) and terminates at point B. The coordinates of point B are estimated as  $J_2 \approx 0.005 \sim 0.0055J_1$ .

which can be understood as a 1D quantum matrix product operator acting on an infinite number of degrees of freedom. In the thermodynamic limit, solving the partition function reduces to finding the leading eigenvalue and leading eigenvectors of the transfer matrix in Fig. 2(e).

Since the transfer matrix  $T$  is non-Hermitian, both the down and up eigen equations should be solved. The solutions to these equations can be accurately found using multi-site variational uniform matrix product state (VUMPS) algorithms [38]. With the up and down leading eigenvectors, various physical quantities including the local observables and the correlation functions can be efficiently calculated. The details of TN construction and calculation of physical quantities can be found in the Supplementary I.B.

**Numerical results.** -Within the framework of TN, the entanglement measure of quantum many-body systems serves as a precise criterion for identifying various phase transitions. For the non-Hermitian transfer matrix under consideration, we employ the generalized entanglement entropy [39, 40] to determine the phase boundary. In Fig. 3(a), the numerical results of the generalized entanglement entropy at  $J_2 = 0.0025J_1$ , with bond dimensions ranging from  $D = 40$  to  $D = 120$  are displayed. The entanglement entropy exhibits a sharp peak and a

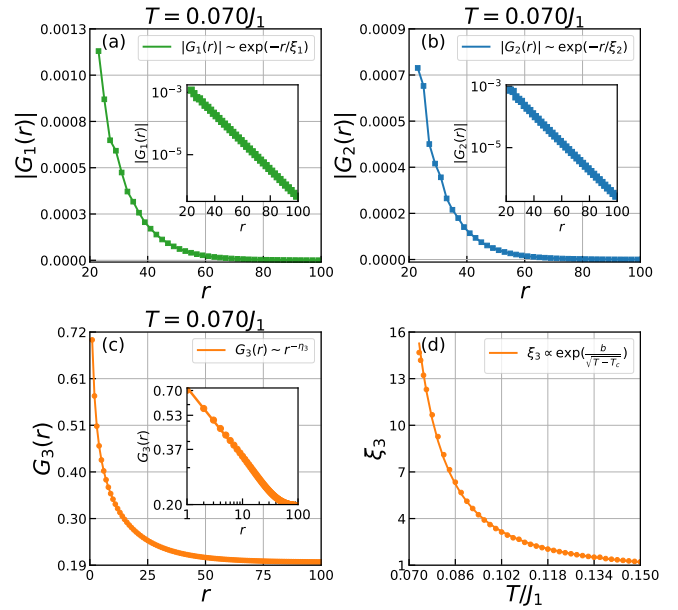


FIG. 4: (a)-(c) The correlation function at  $J_2 = 0.0025J_1, T = 0.070J_1$ . (a) The correlation function of the integer vortices. (b) The correlation function of the  $1/2$  vortices. (c) The correlation function of the  $1/3$  vortices. (d) The extracted correlation length of  $1/3$  fractional vortices.

discontinuous jump, corresponding to a continuous and a discontinuity phase transitions, respectively. The precise transition temperatures can be determined by the extrapolation of the bond dimension. As shown in Fig. 3(b), the lower transition temperature  $T_{c1} \approx 0.035J_1$  remains nearly unchanged as the bond dimension increases, while the higher transition temperature is  $T_{c2} \approx 0.072J_1$ , which is close to the estimated BKT transition temperature driven by  $1/3$  vortex:  $T_{fv} \approx \frac{1}{9}T_v \approx 0.075J_1$ .

For  $J_2 > 0.0055J_1$ , the generalized entanglement entropy exhibits one discontinuous jump only. Then a phase diagram can be calculated and shown in Fig. 3(c), where the low-temperature vortex lattice phase is characterized by QLRO in  $\langle e^{i\theta} \rangle$  and long-range order (LRO) in vorticity variables. When crossing the first-order transition, the vorticity LRO and  $\langle e^{i\theta} \rangle$  QLRO break simultaneously, indicating the melting of the vortex lattice. The extended numerical data is shown in the Supplementary III.A.

The most interesting physics occurs at  $J_2 < 0.0055J_1$ , where a vestigial  $1/3$  vortex-antivortex paired phase emerges. The intermediate phase at  $T_{c1} < T < T_{c2}$  can be characterized by the following correlation function

$$G_n(r) = \langle e^{in(\theta_i - \theta_{i+r})} \rangle = |G_n(r)| e^{i\phi_n(r)}, \quad (10)$$

where  $G_n(r)$  characterizes the correlation behavior of  $1/n$  fractional vortices when  $n > 1$ . In Fig. 4(a)-(b), the correlation functions for both integer vortices and  $1/2$  vortices are calculated at  $T = 0.070J_1$ , and their amplitudes ex-

hibit the exponential decay. Meanwhile, the correlation function for  $\frac{1}{3}$  fractional vortices exhibits a quasi-long-range order

$$G_3(r) = \langle e^{3i(\theta_i - \theta_{i+r})} \rangle \sim r^{-\eta_3}, \quad (11)$$

as depicted in Fig.4(c). Notice that  $G_3(r)$  at large distances shows a tail due to the finite bond dimension. Moreover, above  $T_{c2}$ , a correlation length can be determined with the form of  $G_3(r) \sim \exp(-r/\xi_3)$ . As shown in Fig.4(d), we have

$$\xi_3(T) \sim \exp\left(\frac{b}{\sqrt{T - T_c}}\right), \quad T \rightarrow T_c^+, \quad (12)$$

which suggests the BKT phase transition at  $T_{c2}$  though it is driven by the  $\frac{1}{3}$  vortex unbinding.

The existence of the intermediate phase can be understood from the perspective of topological defects. The first order transition at  $T_{c1}$  is driven by the proliferation of domain walls. Above  $T_{c1}$ , the system is characterized by a network of infinite domain walls intersecting with each other, with  $1/3$  fractional vortices existing as the kinks and the intersections of domain walls. At  $J_2 < 0.005J_1$ , while the free energy cost of the domain walls vanishes, the logarithmic interaction between vortices is still strong enough to bind them in pairs, leading to a fractional vortex pair phase, characterized by QLRO in  $\langle e^{i3\theta} \rangle$ . When further increasing  $J_2$ , once the free energy of the domain wall vanishes, the interaction between fractional vortices is also not strong enough to bind them in pairs. Consequently, the fractional vortex also unbind at the same temperature and the intermediate phase vanishes.

**Conclusion.** -In the context of superconductor phase fluctuation, the QLRO of  $\langle e^{i\theta} \rangle$  corresponds to the global phase coherence of ordinary  $2e$  Cooper pairs, while the QLRO of  $\langle e^{i3\theta} \rangle$  corresponds to the global phase coherence of three pairs of Cooper pairs. The intermediate phase between  $T_{c1}$  and  $T_{c2}$  can be interpreted as a phase referred to as the charge- $6e$  ordered coherent phase, which exhibits global phase coherence between three pairs of Cooper pairs, in the absence of phase coherence between normal  $2e$  Cooper pairs. Just as the QLRO of  $\langle e^{i\theta} \rangle$  gives rise to the flux quantization of  $\frac{h}{2e}$  [41–43], the QLRO of  $\langle e^{i3\theta} \rangle$  also directly accounts for the flux quantization of  $\frac{h}{6e}$ . When an external magnetic field is applied, the superconducting state couples with the gauge field through minimal coupling:  $H \sim |(-i\hbar\nabla - 2eA)\psi|^2$ . In ring devices made of  $\text{AV}_3\text{Sb}_5$ , when the magnetic flux equals  $\frac{1}{3}$  flux quanta,  $\frac{1}{3}$  vortices, which induce a phase gradient  $\int \nabla\theta \cdot dl = \frac{2e}{\hbar} \int A \cdot dl = \frac{2\pi}{3}$ , will be excited from the state to minimize the free energy of the system, giving rise to oscillatory behavior in units of  $\frac{h}{6e}$  [12].

In summary, we have proposed that the  $3Q$  PDW states observed in  $\text{AV}_3\text{Sb}_5$  can be effectively described by  $\psi_{\text{kagome}}$  states, and suggested that the superconducting

fluctuations of these states can be captured by the  $J_1 - J_2$  XY model on a kagome lattice with the nearest-neighbor and next nearest-neighbor AF couplings. Moreover, our findings indicate that when  $J_2 < 0.005J_1$ , a charge- $6e$  phase condensed state can emerge, providing a plausible explanation for the observed superconducting fluctuation region in  $\text{AV}_3\text{Sb}_5$ .

**Acknowledgments.** -The authors are very grateful to Ziqiang Wang and Feng-Feng Song for their stimulating discussions. The research is supported by the National Key Research and Development Program of China (Grant No. 2023YFA1406400).

---

\* Electronic address: gmzhang@tsinghua.edu.cn

- [1] B. R. Ortiz, L. C. Gomes, J. R. Morey, M. Winiarski, M. Bordelon, J. S. Mangum, I. W. H. Oswald, J. A. Rodriguez-Rivera, J. R. Neilson, S. D. Wilson, et al., *Phys. Rev. Mater.* **3**, 094407 (2019), URL <https://link.aps.org/doi/10.1103/PhysRevMaterials.3.094407>.
- [2] B. R. Ortiz, S. M. L. Teicher, Y. Hu, J. L. Zuo, P. M. Sarte, E. C. Schueller, A. M. M. Abeykoon, M. J. Krogstad, S. Rosenkranz, R. Osborn, et al., *Phys. Rev. Lett.* **125**, 247002 (2020), URL <https://link.aps.org/doi/10.1103/PhysRevLett.125.247002>.
- [3] Y.-X. Jiang, J.-X. Yin, M. M. Denner, N. Shumiya, B. R. Ortiz, G. Xu, Z. Guguchia, J. He, M. S. Hossain, X. Liu, et al., *Nature Materials* **20**, 1353 (2021).
- [4] Z. Liang, X. Hou, F. Zhang, W. Lan, P. Wu, Z. Zhang, F. Yu, J.-J. Ying, K. Jiang, L. Shan, et al., *Physical Review X* **11**, 031026 (2021).
- [5] H. Li, T. T. Zhang, T. Yilmaz, Y. Y. Pai, C. E. Marvinney, A. Said, Q. W. Yin, C. S. Gong, Z. J. Tu, E. Vescovo, et al., *Physical Review X* **11**, 031050 (2021).
- [6] B. R. Ortiz, S. M. L. Teicher, L. Kautzsch, P. M. Sarte, N. Ratcliff, J. Harter, J. P. C. Ruff, R. Seshadri, and S. D. Wilson, *Physical Review X* **11**, 041030 (2021).
- [7] H. Luo, Q. Gao, H. Liu, Y. Gu, D. Wu, C. Yi, J. Jia, S. Wu, X. Luo, Y. Xu, et al., *Nature Communications* **13**, 273 (2022).
- [8] Y. Hu, X. Wu, B. R. Ortiz, X. Han, N. C. Plumb, S. D. Wilson, A. P. Schnyder, and M. Shi, *Physical Review B* **106**, L241106 (2022).
- [9] M. Kang, S. Fang, J.-K. Kim, B. R. Ortiz, S. H. Ryu, J. Kim, J. Yoo, G. Sangiovanni, D. Di Sante, B.-G. Park, et al., *Nature Physics* **18**, 301 (2022).
- [10] K. Nakayama, Y. Li, T. Kato, M. Liu, Z. Wang, T. Takahashi, Y. Yao, and T. Sato, *Physical Review X* **12**, 011001 (2022).
- [11] H. Chen, H. Yang, B. Hu, Z. Zhao, J. Yuan, Y. Xing, G. Qian, Z. Huang, G. Li, Y. Ye, et al., *Nature* **599**, 222 (2021).
- [12] J. Ge, P. Wang, Y. Xing, Q. Yin, A. Wang, J. Shen, H. Lei, Z. Wang, and J. Wang, *Phys. Rev. X* **14**, 021025 (2024), URL <https://link.aps.org/doi/10.1103/PhysRevX.14.021025>.
- [13] T. Le, Z. Pan, Z. Xu, J. Liu, J. Wang, Z. Lou, Z. Wang, Y. Yao, C. Wu, and X. Lin, *Evidence for chiral superconductivity in kagome superconductor  $\text{csv}3\text{sb}5$*  (2023), 2309.00264.

- [14] M. M. Denner, R. Thomale, and T. Neupert, Phys. Rev. Lett. **127**, 217601 (2021), URL <https://link.aps.org/doi/10.1103/PhysRevLett.127.217601>.
- [15] J.-W. Dong, Z. Wang, and S. Zhou, Phys. Rev. B **107**, 045127 (2023), URL <https://link.aps.org/doi/10.1103/PhysRevB.107.045127>.
- [16] M. R. Beasley, J. E. Mooij, and T. P. Orlando, Phys. Rev. Lett. **42**, 1165 (1979), URL <https://link.aps.org/doi/10.1103/PhysRevLett.42.1165>.
- [17] V. J. Emery and S. A. Kivelson, Nature **374**, 434 (1995).
- [18] E. W. Carlson, S. A. Kivelson, V. J. Emery, and E. Manousakis, Phys. Rev. Lett. **83**, 612 (1999), URL <https://link.aps.org/doi/10.1103/PhysRevLett.83.612>.
- [19] Q. Li, M. Hücker, G. D. Gu, A. M. Tsvelik, and J. M. Tranquada, Phys. Rev. Lett. **99**, 067001 (2007), URL <https://link.aps.org/doi/10.1103/PhysRevLett.99.067001>.
- [20] V. L. Berezinsky, Sov. Phys. JETP **32**, 493 (1971).
- [21] J M Kosterlitz and D J Thouless, Journal of Physics C: Solid State Physics **6**, 1181 (1973).
- [22] J. M. Kosterlitz, Journal of Physics C: Solid State Physics **7**, 1046 (1974), URL <https://dx.doi.org/10.1088/0022-3719/7/6/005>.
- [23] D. F. Agterberg, M. Geracie, and H. Tsunetsugu, Phys. Rev. B **84**, 014513 (2011), URL <https://link.aps.org/doi/10.1103/PhysRevB.84.014513>.
- [24] S. Zhou and Z. Wang, Nature Communications **13**, 7288 (2022).
- [25] Z. Pan, C. Lu, F. Yang, and C. Wu, *Frustrated superconductivity and "charge-6e" ordering* (2022), 2209.13745.
- [26] A. Vallat and H. Beck, Phys. Rev. B **50**, 4015 (1994), URL <https://link.aps.org/doi/10.1103/PhysRevB.50.4015>.
- [27] S. Teitel and C. Jayaprakash, Phys. Rev. Lett. **51**, 1999 (1983), URL <https://link.aps.org/doi/10.1103/PhysRevLett.51.1999>.
- [28] D. H. Lee, R. G. Caffisch, J. D. Joannopoulos, and F. Y. Wu, Phys. Rev. B **29**, 2680 (1984), URL <https://link.aps.org/doi/10.1103/PhysRevB.29.2680>.
- [29] S. E. Korshunov and G. V. Uimin, Journal of Statistical Physics **43**, 1 (1986), URL <https://doi.org/10.1007/BF01010569>.
- [30] S. E. Korshunov, Phys. Rev. Lett. **88**, 167007 (2002), URL <https://link.aps.org/doi/10.1103/PhysRevLett.88.167007>.
- [31] T. Obuchi and H. Kawamura, Journal of the Physical Society of Japan **81**, 054003 (2012).
- [32] F.-F. Song, T.-Y. Lin, and G.-M. Zhang, Phys. Rev. B **108**, 224404 (2023), URL <https://link.aps.org/doi/10.1103/PhysRevB.108.224404>.
- [33] D. A. Huse and A. D. Rutenberg, Phys. Rev. B **45**, 7536 (1992), URL <https://link.aps.org/doi/10.1103/PhysRevB.45.7536>.
- [34] S. E. Korshunov, Phys. Rev. B **65**, 054416 (2002), URL <https://link.aps.org/doi/10.1103/PhysRevB.65.054416>.
- [35] F.-F. Song and G.-M. Zhang, Phys. Rev. B **105**, 134516 (2022), URL <https://link.aps.org/doi/10.1103/PhysRevB.105.134516>.
- [36] F.-F. Song and G.-M. Zhang, Phys. Rev. B **108**, 014424 (2023), URL <https://link.aps.org/doi/10.1103/PhysRevB.108.014424>.
- [37] F. Kakizawa, T. Misawa, and H. Shinaoka, *Monte carlo study on low-temperature phase diagrams of the  $j_1$ - $j_2$  classical xy kagome antiferromagnet* (2023), 2310.15811.
- [38] A. Nietner, B. Vanhecke, F. Verstraete, J. Eisert, and L. Vanderstraeten, Quantum **4**, 328 (2020), ISSN 2521-327X, URL <https://doi.org/10.22331/q-2020-09-21-328>.
- [39] Y.-T. Tu, Y.-C. Tzeng, and P.-Y. Chang, SciPost Phys. **12**, 194 (2022), URL <https://scipost.org/10.21468/SciPostPhys.12.6.194>.
- [40] W. Tang, F. Verstraete, and J. Haegeman, *Matrix product state fixed points of non-hermitian transfer matrices* (2023), 2311.18733.
- [41] R. Doll and M. Nöbauer, Phys. Rev. Lett. **7**, 51 (1961), URL <https://link.aps.org/doi/10.1103/PhysRevLett.7.51>.
- [42] N. Byers and C. N. Yang, Phys. Rev. Lett. **7**, 46 (1961), URL <https://link.aps.org/doi/10.1103/PhysRevLett.7.46>.
- [43] B. S. Deaver and W. M. Fairbank, Phys. Rev. Lett. **7**, 43 (1961), URL <https://link.aps.org/doi/10.1103/PhysRevLett.7.43>.